

# The Lugiato-Lefever equation driven by a double tightly focused pump

Mateus C. P. dos Santos<sup>1</sup>, Shatrughna Kumar<sup>2</sup>, Wesley B. Cardoso<sup>3</sup>, and Boris A. Malomed<sup>2,4</sup>

<sup>1</sup>*Federal Institute of Maranhão, IFMA-PPGEM, 65030-005, São Luís, Maranhão, Brazil*

<sup>2</sup>*Department of Physical Electronics, School of Electrical Engineering, Faculty of Engineering, and Center for Light-Matter Interaction, Tel Aviv University, Tel Aviv 69978, Israel*

<sup>3</sup>*Instituto de Física, Universidade Federal de Goiás, 74.690-900, Goiânia, Goiás, Brazil and*

<sup>4</sup>*Instituto de Alta Investigación, Universidad de Tarapacá, Casilla 7D, Arica, Chile*

We introduce a model of an optical cavity based on the one-dimensional Lugiato-Lefever (LL) equation, which includes the pump represented by a symmetric pair of tightly localized “hot spots” (HSs) with phase shift  $\chi$  between them, and self-focusing or defocusing cubic nonlinearity. Families of bound states, pinned to the double HS, are found in the system’s parameter space. They feature the effect of the symmetry breaking (SB) between peaks pinned to individual HSs, provided that the phase shift takes values  $0 < \chi < \pi$ , and the LL equation includes the loss term. The SB, which is explained analytically, takes place in the full LL model and its linearized version alike. The same phenomenology is also explored in the framework of the LL equation with the double HS and quintic self-focusing. In that case, there are stable symmetric and asymmetric bound states, in spite of the presence of the background instability driven by the critical collapse.

## I. INTRODUCTION

A fundamental property of nonlinear photonic systems, both conservative and dissipative ones, is that the stable balance between the linear diffraction and/or dispersion and nonlinear self-focusing may support many species of self-trapped states in the form of solitons [1, 2]. In dissipative systems, the existence of solitons also requires the balance between the intrinsic loss and externally applied gain or pump [3, 4]. Detailed theoretical and experimental studies of dissipative solitons have been carried out in various setups, in which the background loss is balanced by gain, such as in lasing media. Such systems are typically modelled by one- and two-dimensional (1D and 2D) equations of the complex Ginzburg-Landau (CGL) type [5, 6].

In externally driven nonlinear optical systems, the losses are compensated by the pump in the form of illuminating laser beams. The fundamental model of such passive systems is supplied by the Lugiato-Lefever (LL) equations [7]. This class of models was theoretically analyzed in many forms, including 1D and 2D ones [9–12]. They predict pattern formation with diverse applications in nonlinear optics and laser physics [8]–[12]. Among these applications, extremely important ones are the generation of Kerr solitons and frequency combs in passive cavities [13]–[27]. The generation of terahertz radiation is another significant effect predicted by the LL equation [28].

Usually, LL models are considered with the spatially uniform pump, which is appropriate for most experimental realizations. On the other hand, the consideration of the LL equations with a localized pump is relevant too, as it is an adequate model for passive optical cavities driven by tightly focused laser beams. Note that strictly localized states can be predicted only in the case of a localized pump, while the spatially uniform pump necessarily gives rise to states existing on top of a nonzero background field. In this context, analytical solutions of the 1D LL equations with the focused pump represented by a delta-function of coordinate  $x$  (“hot spot”, HS) were obtained in Ref. [29] (the tightly localized gain term  $\sim \delta(x)$  makes it also possible to produce exact solutions for pinned modes in the framework of CGL equations [34, 35]). The same work [29] reported approximate solutions of the 2D LL equation with the tightly-focused Gaussian-shaped 2D pump.

Solutions for localized states that represent robust pixels with zero background were obtained in the framework of the 2D LL equation [30], that included the spatially uniform pump, cubic self-interaction, and a tightly-confining harmonic-oscillator potential (which provided the full localization, in spite of the action of the uniform pump). Recently, classes of stable 2D solutions were reported in the framework of the LL equation with a vorticity-carrying spatially localized pump [31].

The next natural step in the studies of localized pumped modes, which is the subject of the present work, is to consider the LL equation with a set of two mutually symmetric HSs, with a phase shift  $\chi$  between them, which represents an experimentally relevant setup for the passive cavity driven by a symmetric pair of tightly focused beams. This setup essentially expands the variety of localized states produced by the LL model, such as double pixels. In particular, the solutions demonstrate symmetry breaking (SB) of the established states supported by the underlying symmetric HS pair, provided that the phase shift takes values  $0 < \chi < \pi$ , and the LL equation includes the loss term. The SB takes place in the framework of both the full LL equation and its linearized version, the basic features of the SB phenomenology being explained here analytically. We also perform the analysis of symmetric and asymmetric states pinned to the double HS in the framework of the 1D LL equation with quintic self-focusing. In the

latter case, stable bound states are found in spite of the presence of the underlying instability driven by the critical collapse [32, 33].

The presentation in the paper is arranged as follows. The main model, based on the cubic LL equation with the double HS, is introduced in Section 2, which also includes analytical results, such as the explanation of the SB phenomenology. Numerical results are reported, in a systematic form, in Section 3. The quintic-LL model with the double HS is addressed, by means of numerical methods, in Section 4. The paper is concluded by Section 5.

## II. THE MODEL

### A. The Lugiato-Lefever (LL) equation with the cubic nonlinearity and a pair of hot spots (HSs)

We consider the LL equation for complex amplitude  $u(x, t)$  of the optical field in the passive 1D cavity with the cubic nonlinearity (the quintic nonlinearity is considered below) and a pair of spatially separated HSs, which represent tightly focused pump beams in the form of delta-functions [34, 35]:

$$\frac{\partial u}{\partial t} = -\alpha u + \frac{i}{2} \frac{\partial^2 u}{\partial x^2} + i\sigma (|u|^2 - \eta^2) u + \epsilon \left[ e^{-i\chi/2} \delta \left( x + \frac{l}{2} \right) + e^{+i\chi/2} \delta \left( x - \frac{l}{2} \right) \right]. \quad (1)$$

Here  $\alpha > 0$  is the loss parameter,  $\sigma = +1$  and  $-1$  corresponds, respectively, to the self-focusing and defocusing Kerr (cubic) nonlinearity, real  $\epsilon > 0$  is the strength of each pump beam,  $l$  and  $\chi$  are the separation and phase shift between them, and parameter  $\eta^2$ , which defines the cavity mismatch, may be positive or negative. In the experiment, phase shift  $\chi$  can be readily imposed by passing one pump beam through a phase plate. The case of  $\eta^2 > 0$  is favorable for the formation of soliton-like states, as the respective version of Eq. (1) is similar to the nonlinear Schrödinger (NLS) equation with the cubic self-focusing nonlinearity.

The set of two delta-functions and SB in this context were previously studied in the framework of the conservative model, based on the NLS equation [36]. Here, a new feature is phase-shift  $\chi$  between the two HSs, which has no natural counterpart in the NLS and CGL equations. The presence of the latter parameter leads to a new effect, in the form of the symmetry breaking (SB) in stable stationary states supported by the symmetric HS pair. Indeed, the symmetry of the solution with respect to the coordinate reflection,  $x \rightarrow -x$ , makes it necessary to replace  $\chi$  by  $-\chi$ , which requires the application of the complex conjugation to the time-independent version Eq. (1). However, the presence of the loss term  $-\alpha u$  in the equation breaks the invariance of the equation with respect to this transformation.

Stationary solutions of Eq. (1) are characterized by values of the total power (alias norm),

$$\begin{aligned} P &= \int_{-\infty}^{+\infty} |u(x)|^2 dx \equiv P_+ + P_-, \\ P_+ &= \int_0^{+\infty} |u(x)|^2 dx, \quad P_- = \int_{-\infty}^0 |u(x)|^2 dx. \end{aligned} \quad (2)$$

The main issue to consider here is the SB (symmetry breaking) of stationary localized patterns pinned to the symmetric HS pair, which takes place in the case of  $P_+ \neq P_-$ , and is characterized by the respective parameter,

$$\text{SB} \equiv \frac{P_+ - P_-}{P_+ + P_-}. \quad (3)$$

The numerical solution of Eq. (1) was performed by means of the fourth-order Runge-Kutta algorithm, based on the Fourier spectral method [38], replacing the ideal delta-functions by the regularized ones,

$$\tilde{\delta}(x) = \frac{1}{\sqrt{\pi\xi}} \exp\left(-\frac{x^2}{\xi^2}\right), \quad (4)$$

with  $\xi$  small enough. The computations were performed with  $\xi = 0.05$

### B. Analytical approximations

In the case of the self-focusing nonlinearity,  $\sigma > 0$ , and  $\eta^2 > 0$ , localized solutions pinned to the single delta-function pump can be approximately found in the framework of the perturbation theory, assuming that  $\alpha$  and  $\epsilon$  are

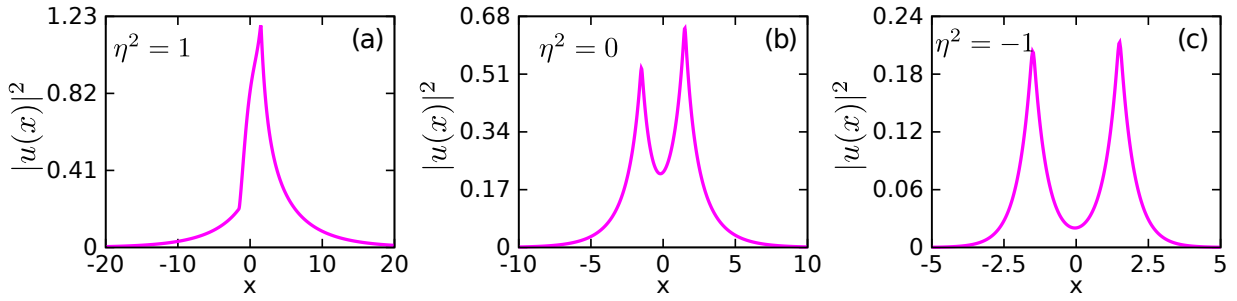


FIG. 1. Stationary profiles obtained numerically from Eq. (1) for  $\eta^2 = 1, 0$ , and  $-1$ . The other parameters are  $\alpha = 0.1, \epsilon = 0.5, \chi = \pi/2, \sigma = -0.5$  and  $l = 3$ .

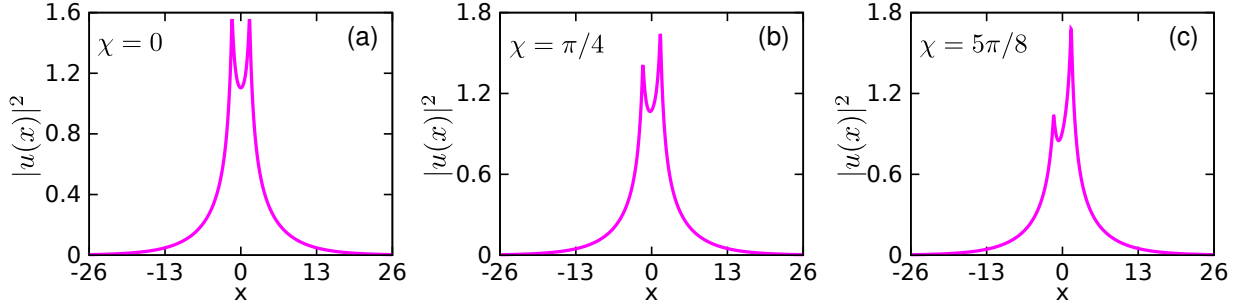


FIG. 2. Symmetric and asymmetric stationary profiles obtained numerically from Eq. (1) for different values of the phase shift  $\chi$  between the two HSS. The other parameters are  $\alpha = 0.1, \epsilon = 0.7, \eta^2 = 1, \sigma = -0.5$  and  $l = 3$ .

small parameters. Setting, for this purpose,  $\sigma = \eta^2 = 1$ , the approximate solution can be taken as the NLS soliton,

$$u_{\text{sol}} \approx \sqrt{2} \exp\left(i\zeta \mp i\frac{\chi}{2}\right) \text{sech}\left(\sqrt{2}\left(x \pm \frac{l}{2}\right)\right), \quad (5)$$

with phase shift  $\zeta$  determined by the power-balance condition between the pump and loss:

$$\frac{dP}{dt} = 2\epsilon \cos \zeta \cdot A - 2\alpha P = 0, \quad (6)$$

where  $A \equiv \sqrt{2}$  is the amplitude of soliton (5), and  $P \equiv 2\sqrt{2}$  is its power. Thus, Eq. (6) yields

$$\cos \zeta = 2\alpha/\epsilon. \quad (7)$$

Obviously, this solution exists under the condition of  $\cos \zeta \leq 1$ , i.e.,

$$\epsilon \geq 2\alpha. \quad (8)$$

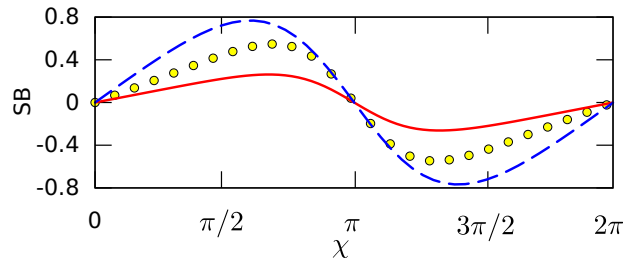


FIG. 3. The asymmetry ratio SB, defined as per Eq. (3) vs.  $\chi$ , for the system with the self-repulsive sign of the nonlinearity,  $\sigma = -0.1, \epsilon = 0.1, \alpha = 0.1$ , and  $l = 3$ . The results represented by the dashed lines, yellow circles, and red solid lines pertain to  $\eta^2 = +1, 0$  and  $-1$ , respectively.

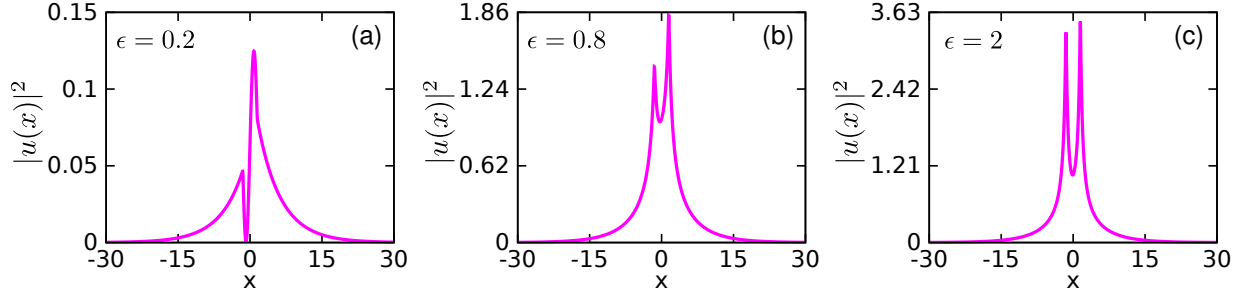


FIG. 4. Stationary profiles obtained numerically from Eq. (1) for different values of the pump strength  $\epsilon$ . The other parameters are  $\alpha = 0.1$ ,  $\chi = \pi/2$ ,  $\eta^2 = 1$ ,  $\sigma = -0.5$  and  $l = 3$ .

On the other hand, it is also possible to construct approximate small-amplitude analytical solutions as those produced by the linearized version of Eq. (1). In the case of  $\sigma\eta^2 > 0$ , the latter equation with a small loss coefficient  $\alpha$  admits the existence of modes tightly pinned to the HS. Then, it is easy to find the respective small-amplitude stationary solution of Eq. (1) a vicinity of each HS (provided that separation  $l$  between them is very large):

$$u_{\text{lin}}^{(\text{tight})} \approx -\frac{i\epsilon}{\sqrt{2\sigma\eta}} \exp\left(\mp i\frac{\chi}{2} - \sqrt{2\sigma\eta^2} \left|x \pm \frac{l}{2}\right|\right), \quad (9)$$

with power

$$P_{\text{lin}}^{(\text{tight})} \approx \frac{\epsilon^2}{(2\sigma\eta^2)^{3/2}} \quad (10)$$

( $\sigma$  and  $\eta^2$  are kept as free parameters here, rather than setting them equal to  $\pm 1$  by means of scaling). As said above, the linearized solution (9) does not depend on the loss parameter  $\alpha$  if it is small enough,  $\alpha \ll \sigma\eta^2$ .

In the opposite case of  $\sigma\eta^2 < 0$  and small  $\alpha \ll -\sigma\eta^2$ , the linearized version of Eq. (1) also supports a bound state, which, however, is a loosely localized one, unlike the tightly bound state (9):

$$u_{\text{lin}}^{(\text{loose})} \approx -\frac{\epsilon}{\sqrt{-2\sigma\eta^2}} \exp\left(\mp i\frac{\chi}{2} - \left(\frac{\alpha}{\sqrt{-2\sigma\eta^2}} + i\sqrt{-2\sigma\eta^2}\right) \left|x \pm \frac{l}{2}\right|\right), \quad (11)$$

whose power is much larger than that given by Eq. (10), as is proportional to  $\alpha^{-1}$ :

$$P_{\text{lin}}^{(\text{loose})} \approx \frac{\epsilon^2}{\alpha\sqrt{-2\sigma\eta^2}}. \quad (12)$$

Finally, in the case of  $\sigma = 0$ , when Eq. (1) is linear by definition, and the loss term is the dominant one in it, the pinned solution is

$$u_{\text{lin}}^{(\sigma=0)} = \frac{\epsilon(1-i)}{2\sqrt{\alpha}} \exp\left(\mp i\frac{\chi}{2} - \sqrt{\alpha}(1-i) \left|x \pm \frac{l}{2}\right|\right), \quad (13)$$

the respective power being

$$P_{\text{lin}}^{(\sigma=0)} = \frac{\epsilon^2}{2\alpha^{3/2}}. \quad (14)$$

The value (10) of the power pertains to the tightly bound linearized solution (9) for the single delta-functional pump. In the case of the pair of the pumps, defined as in Eq. (1), the linearized solution is a superposition of two fields (9) centered at  $x = \pm l/2$ . The corresponding expression for the total power is

$$(P_{\text{lin}})_{\text{total}} \approx \frac{\epsilon^2}{(\sigma\eta^2)^{3/2}} \left[ \frac{1}{\sqrt{2}} + \left( \frac{1}{\sqrt{2}} + \sqrt{\sigma\eta^2}l \right) e^{-\sqrt{2\sigma\eta^2}l} \cos\chi \right]. \quad (15)$$

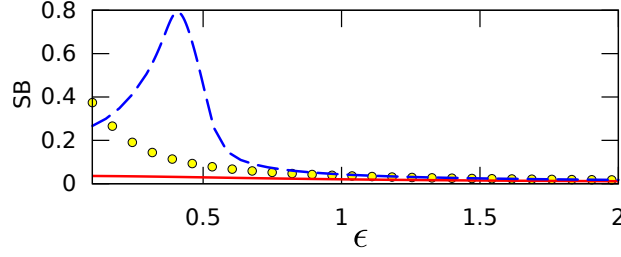


FIG. 5. The asymmetry ratio, SB, defined as per Eq. (3), versus  $\epsilon$  for the self-repulsive system with  $\sigma = -0.5$ ,  $\chi = \pi/2$ ,  $\alpha = 0.1$ , and  $l = 3$ . The blue dashed line, yellow circles, and red solid line pertain to  $\eta^2 = 1, 0$  and  $-1$ , respectively.

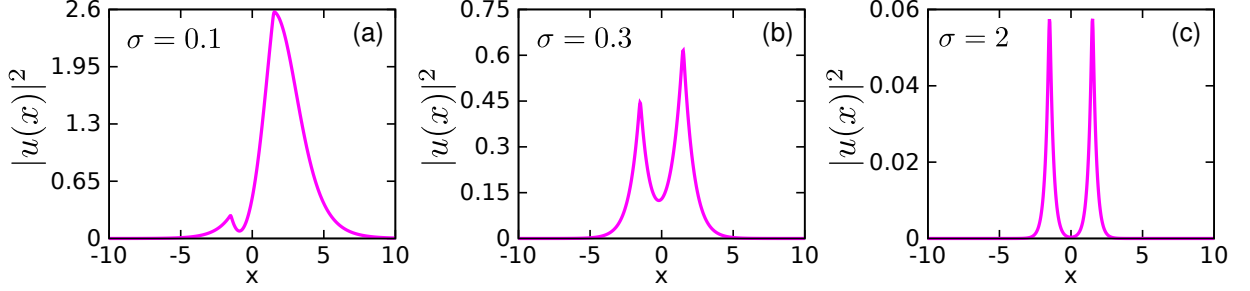


FIG. 6. Symmetric and asymmetric stationary profiles obtained numerically from Eq. (1) for different values of  $\sigma > 0$  with  $\chi = \pi/2$ ,  $\epsilon = 0.5$ ,  $\eta^2 = 1$ ,  $\alpha = 0.1$ , and  $l = 3$ .

In particular, in the limit of  $l \rightarrow \infty$  Eq. (15) yields, naturally, the double value (10) corresponding to the single pump. In the opposite limit,  $l = 0$ , Eq. (15) yields  $(P_{\text{lin}})_{\text{total}}(l = 0) = \sqrt{2}\epsilon^2 \cos^2(\chi/2)$ , which corresponds to the double pump in Eq. (1).

In the limit of  $\alpha \rightarrow 0$ , which corresponds to Eq. (15), the analytical solution of the linearized LL equation (1) does not produce the SB effect. Nevertheless, the solution of the linearized equation exhibits SB if  $\alpha$  is taken into regard. This is easy to see in the limit of  $\sigma = 0$ , when the field created by the single HS is give by Eq. (13). A straightforward calculation produces the following expression for the local power profile created by the two HSs with  $\sigma = 0$ , separated by a finite distance  $l$ :

$$\begin{aligned} |u_{\text{lin}}^{(\sigma=0)}(x;l)|^2 &= \frac{\epsilon^2}{2\alpha} \left[ \sum_{+,-} \exp\left(-2\sqrt{\alpha}\left|x \pm \frac{l}{2}\right|\right) \right. \\ &+ 2 \left. \begin{cases} \exp(-2\sqrt{\alpha}x) \cos(l\sqrt{\alpha} - \chi), & \text{at } x > +l/2, \\ \exp(-\sqrt{\alpha}l) \cos(2\sqrt{\alpha}x - \chi), & \text{at } |x| < l/2, \\ \exp(2\sqrt{\alpha}x) \cos(l\sqrt{\alpha} + \chi), & \text{at } x < -l/2. \end{cases} \right] \end{aligned} \quad (16)$$

It is obvious that the second term in Eq. (16) indeed breaks the symmetry between  $x$  and  $-x$  at  $\chi \neq \pi n$  with integer  $n$  (the respective formal expression for SB (3) is too cumbersome). This SB mechanism is qualitatively similar to the one which explains SB in collisions between solitons with a phase difference between them [37].

### III. NUMERICAL RESULTS

#### A. The shape and stability of the symmetric and asymmetric stationary modes

To produce stationary states admitted by Eq. (1), we ran real-time simulations of this equations, starting from the "vacuum state",  $u(x, t = 0) = 0$ , until the solution would converge to a stationary state. Obviously, the states produced by this approach are stable.

We begin the analysis by studying the effect of  $\eta^2$  on the stationary states. In Fig. 1, we present their profiles obtained with  $\alpha = 0.1$ ,  $\epsilon = 0.5$ ,  $\chi = \pi/2$ ,  $l = 3$  and  $\sigma = -0.5$  (the self-defocusing sign of the nonlinearity), for  $\eta^2 = +1, 0$ , and  $-1$ . In this case, we observe that the asymmetry measure (3) reduces with the decrease of  $\eta^2$ . In

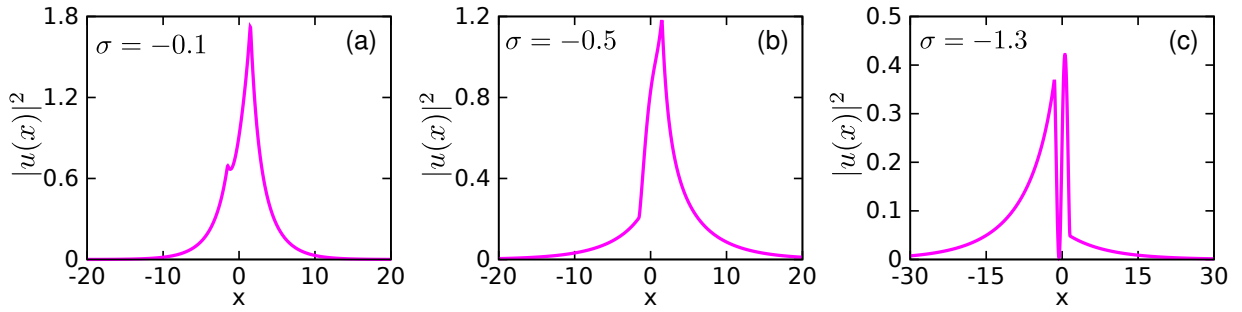


FIG. 7. The same as in Fig. 6, but for the system with the self-repulsion ( $\sigma < 0$ ).

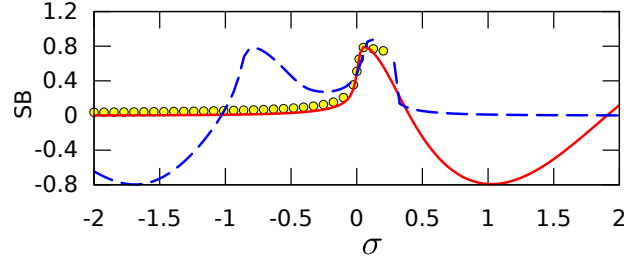


FIG. 8. The asymmetry ratio SB, defined as per Eq. (3) vs.  $\sigma$  for the system with self-repulsion and attraction with  $\chi = \pi/2$ ,  $\epsilon = 0.5$ ,  $\alpha = 0.1$ , and  $l = 3$ . The blue dashed line, yellow circles, and the red solid line correspond to  $\eta^2 = 1, 0$  and  $-1$ , respectively. In the case of the self-attraction, the system does not create stationary states in the wide empty region.

particular, for  $\eta^2 = +1$ , the resulting stationary state yields  $SB = 0.46$ , while for  $\eta^2 = -1$ , a small value  $SB = 0.03$  is obtained. It is also observed that the reduction of  $\eta^2$  leads to a decrease in the amplitude of the stationary modes.

In Fig. 2 we address the dependence of the stationary states on the phase difference  $\chi$  between the pump beams. It is observed that, in agreement with the above-mentioned argument, the states with  $\chi = 0$  (as well as with  $\chi = \pi n$ , with integer  $n$ ) keep the spatial symmetry. On the other hand, the states obtained with the phase shift from interval  $0 < \chi < \pi$  exhibit asymmetry, the size of which depends on the other parameters.

The dependence of the SB parameter on  $\chi$  is presented in Fig. 3, which exhibits the natural sinusoidal behavior with the period of  $2\pi$ , which, naturally, includes positive and negative values. The decrease in  $\eta^2$  leads to reduction of the amplitude of the dependence, the minimum of which corresponds to  $\eta^2 = -1$ .

Figure 4 presents the comparison between power profiles,  $|u(x)|^2$ , for the stationary states obtained with different strengths  $\epsilon$  of the pump beams. Naturally, the power grows with the increase of the pump strength  $\epsilon$ . Furthermore, the profiles drastically alter with the variation of  $\epsilon$ , directly affecting the respective SB value. To complement this analysis, in Fig. 5 we plot the relation between SB and  $\epsilon$ . It is observed that the increase of  $\epsilon$  favors symmetric profiles. This trend is explained by the above-mentioned fact that SB is explained by the loss term  $-au$  in Eq. (1), while the increase of  $\epsilon$  makes the loss term relatively weaker. The same fact explains the presence of nonvanishing SB at  $\epsilon \rightarrow 0$ , which corresponds to the linear limit of Eq. (1).

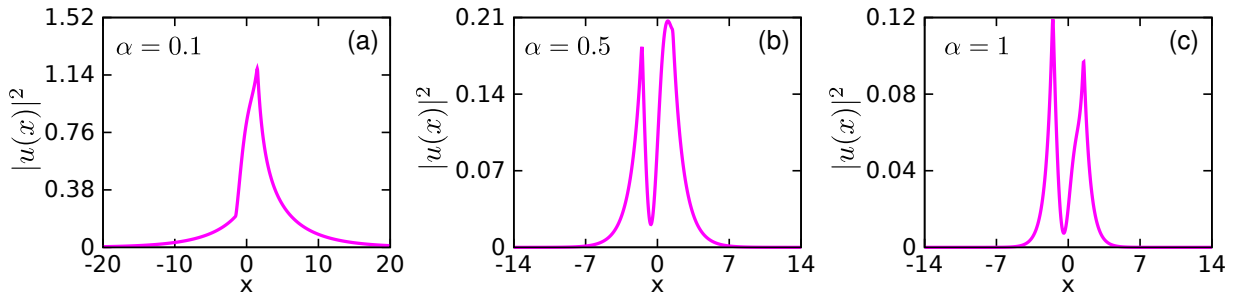


FIG. 9. Asymmetric stationary profiles obtained numerically from Eq. (1) for different values of the loss coefficient  $\alpha$  with  $\chi = \pi/2$ ,  $\epsilon = 0.5$ ,  $\eta^2 = 1$ ,  $\sigma = -0.5$ , and  $l = 3$ .

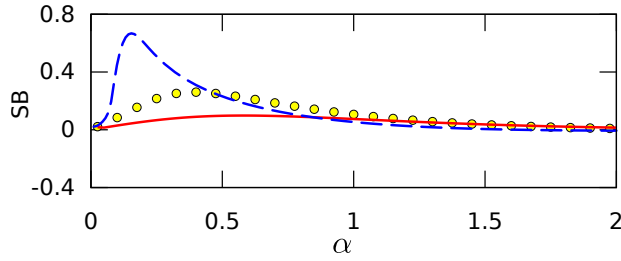


FIG. 10. The asymmetry ratio  $SB$ , defined as per Eq. (3), vs.  $\alpha$  for the system with the self-repulsive nonlinearity, with  $\sigma = -0.5$ ,  $\chi = \pi/2$ ,  $\epsilon = 0.5$ , and  $l = 3$ . The results in blue dashed line, yellow circles and red solid line correspond to  $\eta^2 = 1, 0$  and  $-1$ , respectively.

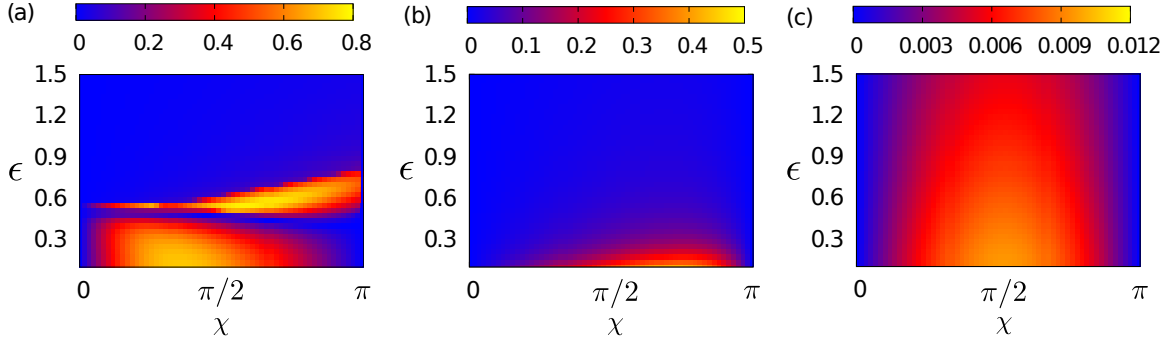


FIG. 11. The chart of the values of  $|SB|$  in the plane of the phase shift  $\chi$  and pump strength  $\epsilon$ , for (a)  $\eta^2 = 1$ , (b)  $\eta^2 = 0$ , and (c)  $\eta^2 = -1$ . The other parameters are  $\alpha = 0.1$ ,  $\sigma = -1$ , and  $l = 3$ .

The increase of the self-interaction strength  $\sigma$  promotes various features of the profile of the stationary states. In general, the increase of  $\sigma > 0$  (self-focusing) drives the profile narrowing. Other effects are observed too, such as the reduction of  $SB$ . Figure 6 shows that the increase of  $\sigma > 0$  transforms the asymmetric state into a narrow symmetric one with well-separated peaks, which is explained by the same argument as presented above: the increase of  $\sigma$  makes the asymmetry-inducing loss term relatively weaker. Additionally, for certain values of  $\epsilon$ , which are detailed below, stationary states are not supported in the in a self-focusing regime, while this phenomenon does not occur in the self-defocusing case ( $\sigma < 0$ ). Different stationary states obtained in this case are presented in Fig. 7. It is observed that the decrease of  $\sigma$  (i.e., increase of  $|\sigma|$ ) promotes wider profiles, which affects the  $SB$ .

In Fig. 8 we present the effect of the self-interaction on  $SB$ . For the profiles obtained with  $\eta^2 = 1$  and  $-1$ , the behavior of the  $SB$  is quite complex, featuring both positive and negative values of  $SB$ . The dependences  $SSB(\sigma)$  is opposite for  $\eta^2 = 1$  and  $\eta^2 = -1$ , as the symmetric states are favored at  $\sigma < 0$  and  $\sigma > 0$  for  $\eta^2 = -1$  and  $1$ , respectively. In particular, the curve  $SSB(\sigma)$  for  $\eta^2 = 1$  features a discontinuity at  $\sigma > 0$  region, where stationary profiles actually do not exist (were not found). For  $\eta^2 = 0$ , the value of  $SSB(\sigma)$  is very small at  $\sigma < 0$ . In the self-defocusing regime, the curve  $SSB(\sigma)$  for  $\eta^2 = 0$  is limited at  $\sigma < 0.3$ , beyond which stationary profile were not found.

The effect of loss parameter  $\alpha$  on the shape of the stationary states is presented in Fig. 9. It is observed that the increase in  $\alpha$  leads to a decrease of the total power  $P$ . In general, the increase in  $\alpha$  reduces  $SB$ . To detail this effect, we explored the change of  $SB$  with the variation of  $\alpha$ . In Fig. 10, it is observed that, in agreement with the above analysis of the solutions of the linearized equation (1),  $SB$  vanishes at  $\alpha = 0$ . At large value of  $\alpha$  the stationary states tend to gradually restore their symmetry. Considering different values of  $\eta^2$ , it is again observed that the lowest values of  $SB$  correspond to  $\eta^2 = -1$ .

## B. The summary of numerical findings

To summarize the findings for  $SB$ , we produce color-coded charts for  $|SB|$  in parameter planes  $(\chi, \epsilon)$ ,  $(\sigma, \epsilon)$ ,  $(\alpha, \epsilon)$ , and  $(l, \epsilon)$ , plotted for  $\eta^2 = 1, 0$ , and  $-1$ . In particular, the range of the phase-shift parameter  $\chi$  is naturally confined to  $0 < \chi < \pi$ .

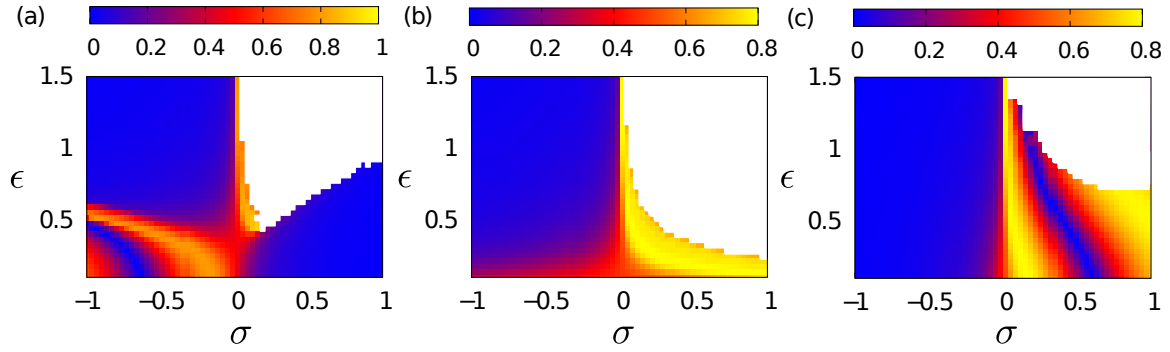


FIG. 12. The chart of the values of  $|SB|$  in the plane of the self-interaction strength  $\sigma$  and pump strength  $\epsilon$ , for (a)  $\eta^2 = 1$ , (b)  $\eta^2 = 0$ , and (c)  $\eta^2 = -1$ . The other parameters are  $\alpha = 0.1$ ,  $\chi = \pi/2$ , and  $l = 3$ . The stationary states were not found in white areas.

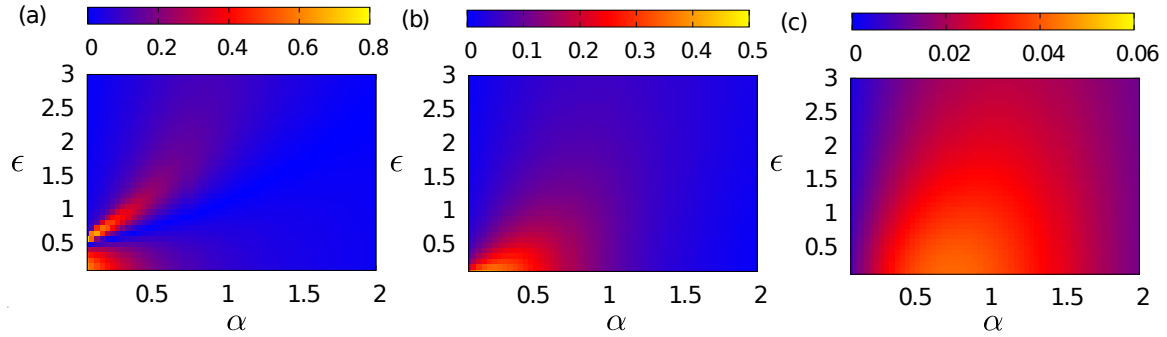


FIG. 13. The chart of the values of  $|SB|$  in the plane of the loss coefficient  $\alpha$  and pump strength  $\epsilon$ , for (a)  $\eta^2 = 1$ , (b)  $\eta^2 = 0$ , and (c)  $\eta^2 = -1$ . The other parameters are  $\sigma = -1$ ,  $\chi = \pi/2$ , and  $l = 3$ .

First, in the chart plotted in the  $(\chi, \epsilon)$  plane for  $\eta^2 = 1$ , it is observed that symmetric profiles are favored for intense pump beams, i.e., for large values of  $\epsilon$ , as already mentioned above. As shown in Fig. 3, the largest values of  $|SB|$  are found in a vicinity of  $\chi = \pi/2$ , in the weak-pump regime (small  $\epsilon$ ). For  $\eta^2 = 0$ , the chart demonstrates strong reduction of the SSB area. In the chart for  $\eta^2 = -1$ , strong attenuation of SB is observed in comparison to the cases of  $\eta^2 = 1$  and 0. Note that, in all the cases, only symmetric profiles are found for  $\chi = 0$  and  $\pi$ , in agreement with the above analysis. These results are displayed in Fig. 11.

In Fig. 12, we present the SB charts in the plane of  $(\sigma, \epsilon)$ . In all the three panels, there are white areas at  $\sigma > 0$  (self-focusing) in which stationary profiles were not found. Further, it is observed that the asymmetry is favored for weak pump beams in the self-defocusing system with  $\eta^2 = 1$ . In the case of  $\eta^2 = 0$ , the SB again occurs mainly for weak beam pumps. On the contrary, for  $\eta^2 = -1$  SB is favored in the self-focusing system. As stressed above, the

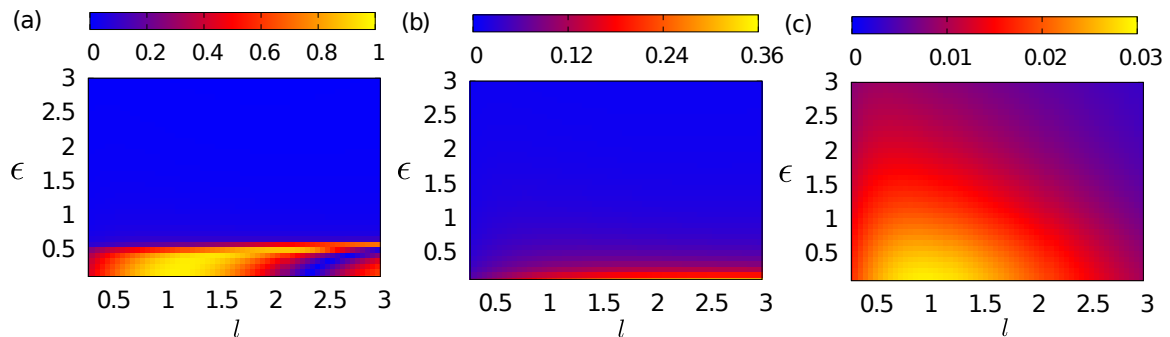


FIG. 14. The chart of the values of  $|SB|$  in the plane of the separation between the delta-functional pumps  $l$  and their strength  $\epsilon$ , for (a)  $\eta^2 = 1$ , (b)  $\eta^2 = 0$ , and (c)  $\eta^2 = -1$ . The other parameters are  $\alpha = 0.1$ ,  $\chi = \pi/2$  and  $\sigma = -1$ .



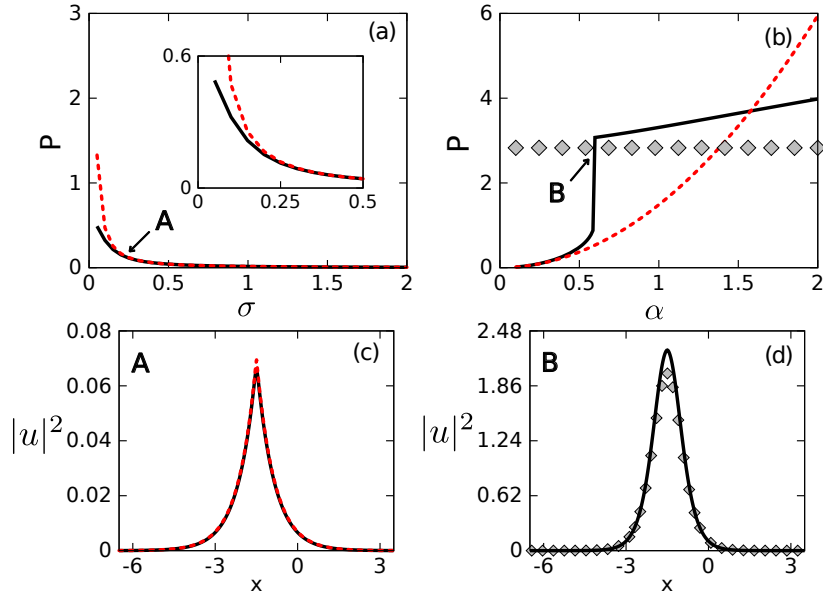


FIG. 15. The comparison between the approximate analytical solutions (9) and (5) and their numerical counterparts found as stationary profiles of Eq. (1) with the single delta-function pump located at  $x = -l/2 \equiv -1.5$ . Panels (a) and (b) display the power  $P$  of the stationary mode vs.  $\sigma$  and  $\alpha$ , respectively. In (c) and (d), we present the comparison between power profiles  $|u(x)|^2$  of the numerically found solutions and their approximate counterparts, corresponding to points **A** ( $\sigma = 0.3$ ) and **B** ( $\alpha = 0.61$ ), respectively. The numerical solution is shown the black solid lines, while the approximations produced by Eqs. (5) and (9) are depicted by the chain of gray diamonds and the red dotted line, respectively. At point **A**, solution (5) is irrelevant, therefore it is not represented in panel (c). For the same reason, solution (9) is not displayed in (d). The results were obtained with  $\epsilon = 2.05\alpha$ ,  $\eta^2 = 1$  and  $\alpha = 0.1$  in (a), and  $\sigma = 1$  in (b).

results demonstrate the persistence of SB in the linearized system, with  $\sigma = 0$ .

The SB charts in the plane of  $(\alpha, \epsilon)$  are shown in Fig. 13. For  $\eta^2 = 1$ , SB occurs solely at  $\alpha < 1$ . In the case of  $\eta^2 = 0$ , SB occurs for small values of the loss coefficient  $\alpha$  in system with weak pump beams. For  $\eta^2 = -1$ , the SB parameter is very small when compared to the results for  $\eta^2 = 1$  and 0.

Next, in Fig. 14 we address the dependence of SB on distance  $l$  between the pump beams. In all cases, the increase of  $l$  leads to attenuation of SB and consequently the obtaining of symmetric profiles. This trend is easily explained by the fact that the asymmetric part of the local-power pattern obtained in Eq. (16) decays exponentially with the increase of  $l$ .

### C. Comparison of analytical and numerical results

It is relevant to check the accuracy of the above-mentioned approximate analytical solutions (5) and (9). To this end, we use stationary profiles produced by the numerical solution of Eq. (1), which includes the single delta-function pump. In Figs. 15(a) and 15(b), we present the comparison of the analytically predicted and numerically found dependences of power  $P$  on nonlinearity strength  $\sigma$  and loss coefficient  $\alpha$ , respectively. In this figure, the pump strength is taken as  $\epsilon = 2.05\alpha$ , to consider the situation close to the existence threshold (8) for the approximate solution (5).

It is seen in Fig. 15(a) that the small-amplitude analytical solution (9) produces the result which is close to its numerically found counterpart, both being virtually identical at  $\sigma > 0.2$ . Further, Fig. 15(b) demonstrates that the same approximate solution (9) predicts the  $P(\alpha)$  dependence which is close to its numerical counterpart at  $\alpha < 0.5$ , exhibiting strong discrepancy at large values of  $\alpha$ .

The soliton-like approximate solution (5) has the constant ( $\alpha$ -independent) power,  $P = 2\sqrt{2}$ , which is shown by the horizontal chain of diamonds in Fig. 15(b). It is seen in this figure that the soliton approximation is irrelevant for small values of  $\alpha$ , but at  $\alpha = 0.6$  the numerical solution suddenly makes a jump to a value close to this constant, differing from it by 8.8%. At larger values of  $\alpha$ , the power of the numerical solution demonstrates a slow growth, so that the analytical prediction, based on the soliton ansatz, remains a roughly relevant one. The comparison between the profiles of the approximate solutions, given by expressions (5) and (9), and their numerically found counterparts

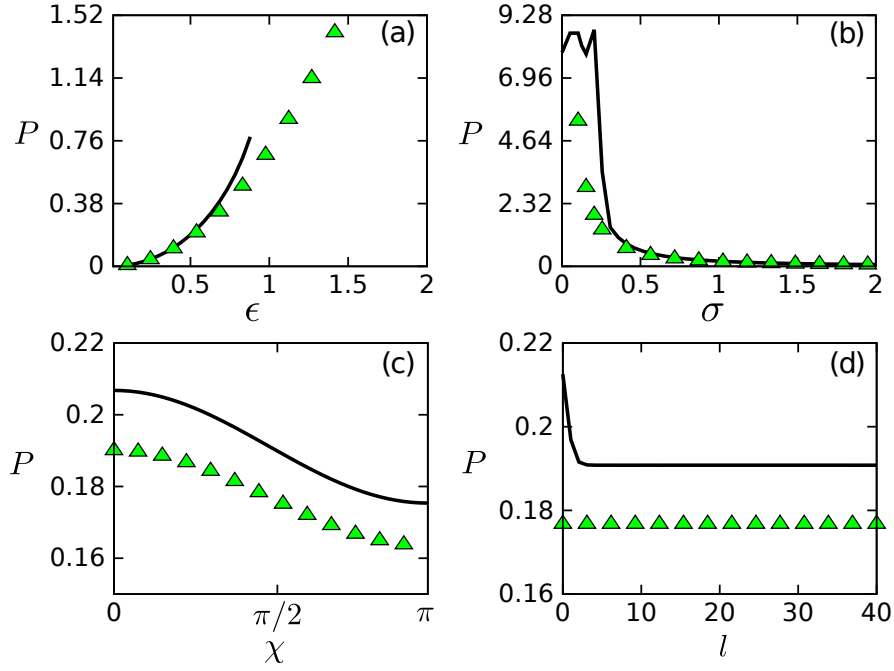


FIG. 16. Dependences of the power on parameters  $\epsilon$ ,  $\sigma$ ,  $\chi$  and  $l$ . The power of the numerical solutions of Eq. (1) with  $\eta^2 = 1$  are displayed by solid black lines, which are compared to the approximate analytical expression  $(P_{\text{lin}})_{\text{total}l}$ , as given by Eq. (15) and plotted by green triangles. The other parameters are: (a)  $\sigma = 1$ ,  $\alpha = 0.1$ ,  $\chi = \pi/2$  and  $l = 3$ ; (b)  $\epsilon = 0.5$ ,  $\alpha = 0.1$ ,  $\chi = \pi/2$  and  $l = 3$ ; (c)  $\sigma = 1$ ,  $\epsilon = 0.5$ ,  $\alpha = 0.1$  and  $l = 3$ ; and (d)  $\sigma = 1$ ,  $\epsilon = 0.5$ ,  $\alpha = 0.1$  and  $\chi = \pi/2$ .

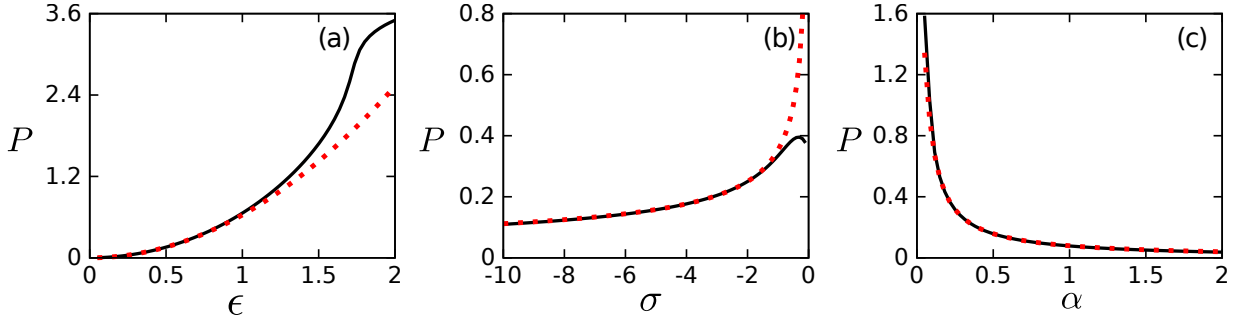


FIG. 17. Dependences of the power on parameters  $\epsilon$ ,  $\sigma$ , and  $\alpha$ . The power of the numerical solutions of Eq. (1) with the single delta-function located at  $l/2$  are displayed by solid black lines, which are compared to the approximate analytical expression  $P_{\text{lin}}^{(\text{loose})}$ , as given by Eq. (12) and plotted by red dotted lines. The other parameters are:  $\eta^2 = 1$  and  $l = 3$  (a)  $\alpha = 0.5$  and  $\sigma = -5$ ; (b)  $\epsilon = 0.5$  and  $\alpha = 0.5$ ; (c)  $\sigma = -5$  and  $\epsilon = 0.5$ .

at points **A** and **B** are shown in Figs. 15(c) and 15(d), respectively.

The above comparison is performed for the LL equation with the single HS. In the case of Eq. (1) with the HS pair, the analytical prediction for the power of small-amplitude (linear) stationary state was derived above in the form of Eq. (15). It is compared to the power of the numerically found symmetric solution in Fig. III B. In Fig. III B(a), we observe that the analytical prediction is close to the numerical results at  $\epsilon < 0.88$ , while at  $\epsilon > 0.88$  stationary numerical solutions were not found. Other panels of Fig. III B demonstrate that the analytical approximation (15) provides a relatively accurate prediction for the parameter dependences of the power. In particular, the values of  $P$  in the dependences  $P(\chi)$  and  $P(l)$ , displayed in panels (c) and (d), differ from their numerically produced counterparts by  $\approx 8\%$ .

In Fig. 17, we illustrate the dependencies of power on the parameters  $\epsilon$ ,  $\sigma$ , and  $\alpha$ . This analysis considers the power of the numerical solutions derived from Eq. (1), with a single delta function located at  $l/2$ , compared to the approximate analytical expression  $P_{\text{lin}}^{(\text{loose})}$ , as defined by Eq. (12). Specifically, from Fig. 17(a), it can be observed that the linear approximation holds valid for small values of  $\epsilon$ . Conversely, Fig. 17(b) demonstrates that as the absolute

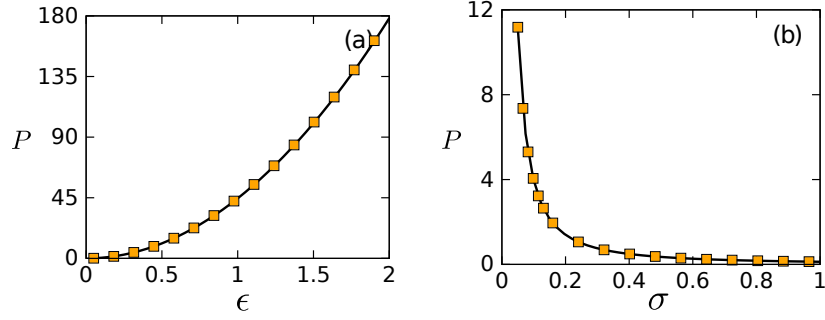


FIG. 18. Dependences of the power on parameters  $\epsilon$  and  $\alpha$ . The power of the numerical solutions of Eq. (1) with the single delta-function are displayed by solid black lines, which are compared to the approximate analytical expression  $P_{lin}^{(\sigma=0)}$ , as given by Eq. (14) and plotted by orange squares. The other parameters are:  $\sigma = 0, \chi = \pi/2$  and  $l = 3$  (a)  $\alpha = 0.05$ ; and (b)  $\epsilon = 0.5$ .

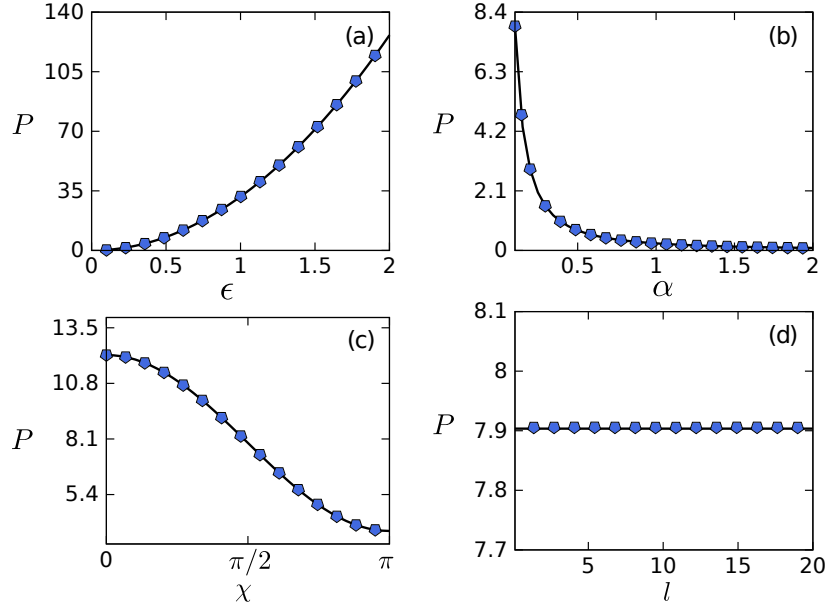


FIG. 19. Dependences of the power on parameters  $\epsilon, \alpha, \chi$  and  $l$ . The power of the numerical solutions of Eq. (1) with  $\eta^2 = 1$  and  $\sigma = 0$  are displayed by solid black lines, which are compared with the power of the approximate analytical solution  $|u_{lin}^{(\sigma=0)}(x; l)|^2$ , as given by Eq. (16) and plotted by blue pentagons. The other parameters are: (a)  $\sigma = 1, \alpha = 0.1, \chi = \pi/2$  and  $l = 3$ ; (b)  $\epsilon = 0.5, \alpha = 0.1, \chi = \pi/2$  and  $l = 3$ ; (c)  $\sigma = 1, \epsilon = 0.5, \alpha = 0.1$  and  $l = 3$ ; and (d)  $\sigma = 1, \epsilon = 0.5, \alpha = 0.1$  and  $\chi = \pi/2$ .

value of negative parameter  $\sigma$  increases, the fit of the linear approximation to the complete result improves. The final panel, Fig. 17(c), illustrates that varying the damping parameter  $\alpha$  - with  $\sigma = -5$  and  $\epsilon = 0.5$  held constant - consistently yields accurate results for the linear approximation.

Subsequently, we present in Fig. 18 the behavior of power as a function of  $\epsilon$  and  $\alpha$  for the approximate analytical expression  $P_{lin}^{(\sigma=0)}$ , given by Eq. (14), compared to the results obtained from the complete equation (Eq. (1)), with a single delta function located at  $l/2$ . Notably, for  $\sigma = 0$ , the approximate solution exhibits similar behavior to the results obtained numerically from Eq. (1).

In the subsequent analyses, we investigate the approximate solutions for the case of a pair of pumps, as defined in Eq. (1). Here, the linearized solution is a superposition of two fields centered at  $x = \pm l/2$ , as described by Eq. (16). In this context, Fig. 19 presents some examples of the power dependence on the system parameters when  $\sigma = 0$ . It can be observed once again that the power behavior of the approximate solution (Eq. (15)) closely matches that produced by the numerical simulations of Eq. (1), demonstrating the robustness of the solution.

The symmetry breaking, as characterized by the function given in Eq. (3), was also analyzed for this approximate solution. In Fig. 20, we display the behavior of the parameter related to the symmetry breaking of the approximate solution, given by Eq. (16), alongside its numerical counterpart obtained from direct simulations of Eq. (1). The

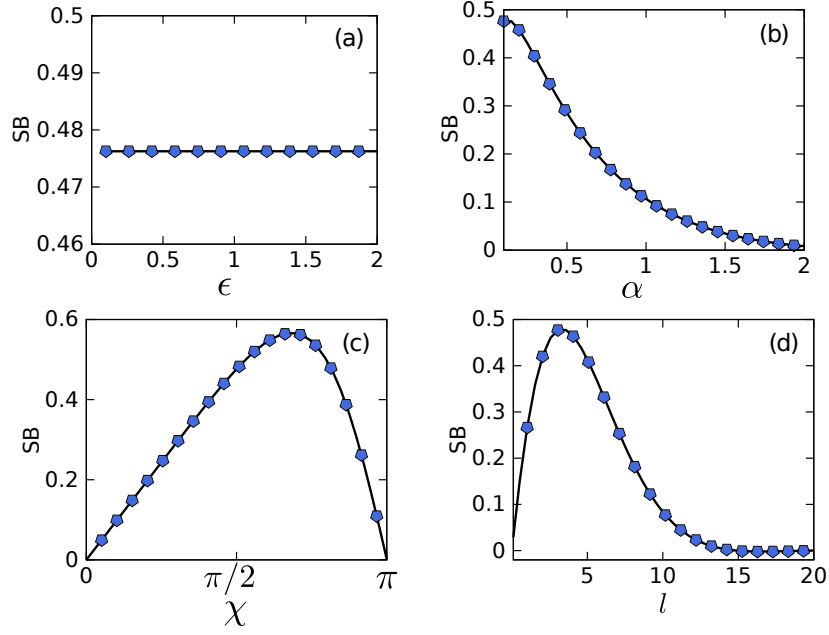


FIG. 20. The same as Fig. 19, but considering the symmetry breaking (SB), given by Eq. (3).

behavior of both solutions is consistent, as evidenced by the panels in Fig. 20, which highlight the behavior for various values of the system parameters.

#### IV. THE DOUBLE-HS SYSTEM WITH THE QUINTIC NONLINEARITY

The quintic self-focusing nonlinearity occurs in many optical materials [39–41], including those which may feature it in a nearly “pure” form, while the cubic term is negligible [42]. This fact suggests a possibility to introduce the LL equation with the quintic nonlinear term [31, 43, 44]. In the present context, we consider the quintic LL equation including the double HS,

$$\frac{\partial u}{\partial t} = -\alpha u + \frac{i}{2} \frac{\partial^2 u}{\partial x^2} + i\sigma (|u|^4 - \eta^4) u + \epsilon \left[ e^{-i\chi/2} \delta \left( x + \frac{l}{2} \right) + e^{i\chi/2} \delta \left( x - \frac{l}{2} \right) \right], \quad (17)$$

with  $\sigma > 0$  and  $\eta^2 > 0$ . cf. its cubic counterpart (1).

On the other hand, a well-known fact is that the quintic self-focusing in 1D waveguides gives rise to the *critical collapse*; accordingly, the family of the *Townes solitons* (TSs) produced by the 1D NLS equation, are completely unstable [45]. TSs are represented by the following exact solution to Eq. (17), with  $\alpha = \epsilon = 0$ :

$$u_{\text{TS}}(x) = \frac{3^{1/4} \eta}{\sqrt{\cosh(2\sqrt{2\sigma} \eta^2 x)}}. \quad (18)$$

Its power is a constant which does not depend on real mismatch  $\eta$ , viz.,  $P_{\text{TS}} = (\pi/2) \sqrt{3/(2\sigma)}$  (the degeneracy of the TS family, i.e., the independence of the power on the phase mismatch, is a fundamental property of TSs [32, 33]).

The instability of the TSs created by the quintic self-focusing suggests a challenging possibility to check if the LL model with the quintic term can support stable localized modes pinned to an HS, or to the double HS, as introduced in Eq. (17). Following the method used above, we performed numerical solutions of Eq. (17) with the zero initial conditions. As a result, families of stable symmetric and asymmetric bound states, pinned to the double HS, have been found. Typical examples of the symmetric and asymmetric stationary profiles are displayed in Fig. 21. In this figure, values of parameters are chosen to be similar to those used in Fig. 6, to highlight differences between the stationary states produced by the cubic and quintic LL equations. In this configuration, stationary profiles are found only for a sufficiently strong quintic nonlinearity, viz., with  $\sigma \geq 0.21$ .

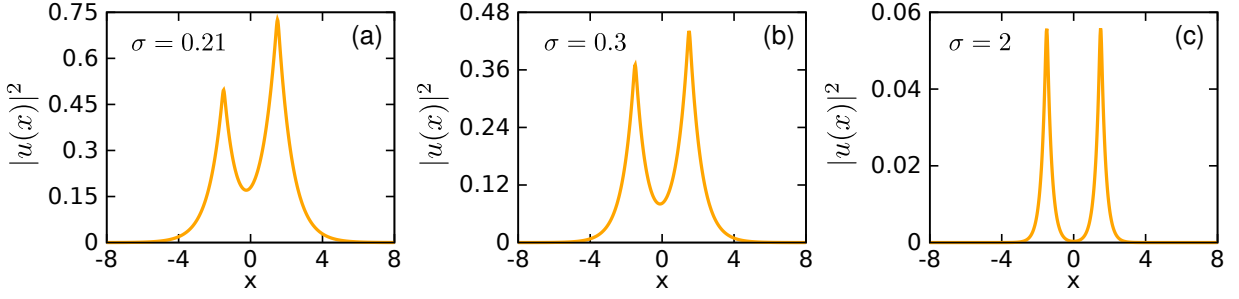


FIG. 21. Profiles of stable stationary states produced by the numerical solution of the quintic LL model (17) for different values of the quintic coefficient  $\sigma > 0$ . The other parameters are  $\alpha = 0.1$ ,  $\chi = \pi/2$ ,  $\eta^4 = 1$ ,  $\epsilon = 0.5$  and  $l = 3$ .

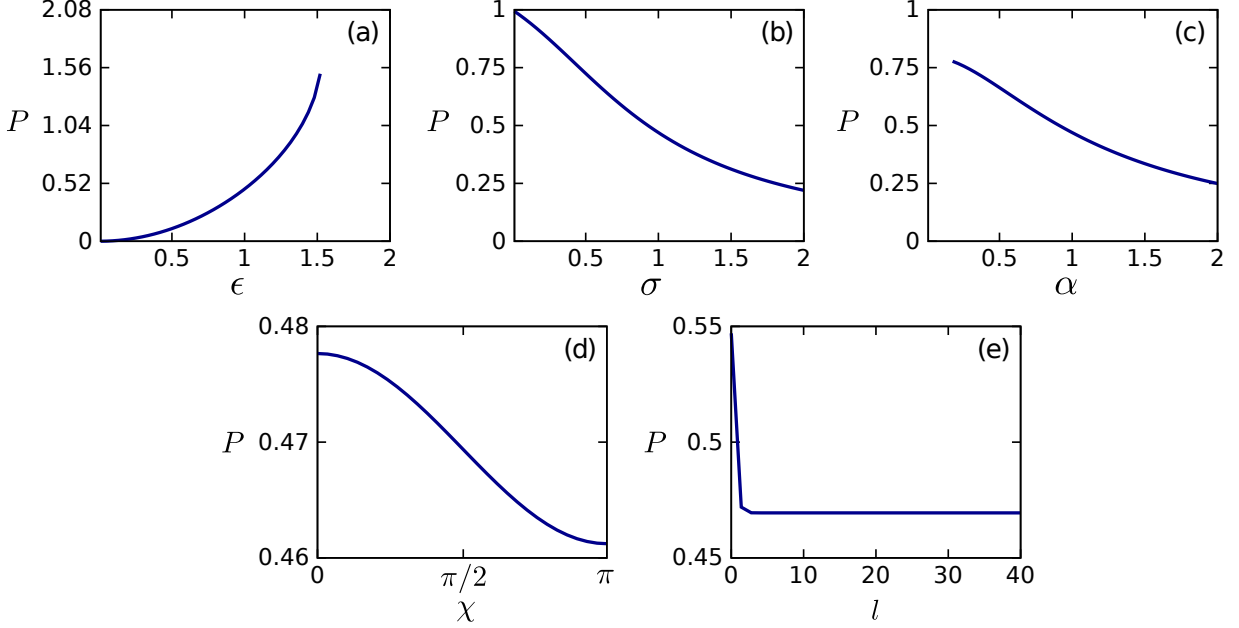


FIG. 22. Power of the stationary states produced by the quintic LL equation (17) with  $\eta^4 = 1$  vs. parameters  $\epsilon$ ,  $\sigma$ ,  $\alpha$ ,  $\chi$  and  $l$ . Other parameters are (a)  $\alpha = 1$ ,  $\sigma = 1$ ,  $\chi = \pi/2$ , and  $l = 3$ ; (b)  $\epsilon = 1$ ,  $\alpha = 1$ ,  $\chi = \pi/2$ , and  $l = 3$ ; (c)  $\epsilon = 1$ ,  $\sigma = 1$ ,  $\chi = \pi/2$ , and  $l = 3$ ; (d)  $\epsilon = 1$ ,  $\sigma = 1$ ,  $\alpha = 1$ , and  $l = 3$ ; (e)  $\epsilon = 1$ ,  $\sigma = 1$ ,  $\alpha = 1$ , and  $\chi = \pi/2$ .

The families of stable stationary states produced by the quintic LL model (17) are characterized, in Fig. 22, by dependences of their power on parameters  $\epsilon$ ,  $\sigma$ ,  $\alpha$ ,  $\chi$ , and  $l$ . Even for a very pump, with  $\epsilon = 0.01$ , we find stationary profiles with  $P = 4 \times 10^{-5}$  in the case displayed in Fig. 22. In the same case, the increase of the pump strength leads to the increase of power. The stationary stable state ceases to exist at  $\epsilon > 1.52$ . In latter case, the bound states develop oscillatory instability, as shown in Fig. 23.

Figures 22(b) and (c) demonstrate that the power of the stationary states decreases with the increase of the quintic and loss coefficients,  $\sigma$  and  $\alpha$ , respectively. In particular, the stable stationary profiles are found, in Fig. 22(c), at  $\alpha \geq 0.17$ , while at  $\alpha < 0.17$  the bound states develop oscillatory instability, similar to that displayed in Fig. 23.

## V. CONCLUSION

We have introduced the one-dimensional LL (Lugiato-Lefever) equation including the self-focusing or defocusing cubic nonlinearity and the symmetric set of two tightly focused pumps (hot spots, HSs), approximated by the delta-function, with the phase shift  $\chi$  between them. Extensive numerical simulations demonstrate the existence of the broad family of stable bound states pinned to the double HS. The bound states are characterized by their power and symmetry or asymmetry between the peaks pinned to the individual HS. The boundary of the onset of SB (symmetry breaking) is identified in the system's parameter space. The bound state always remains symmetric for  $\chi = 0$  and

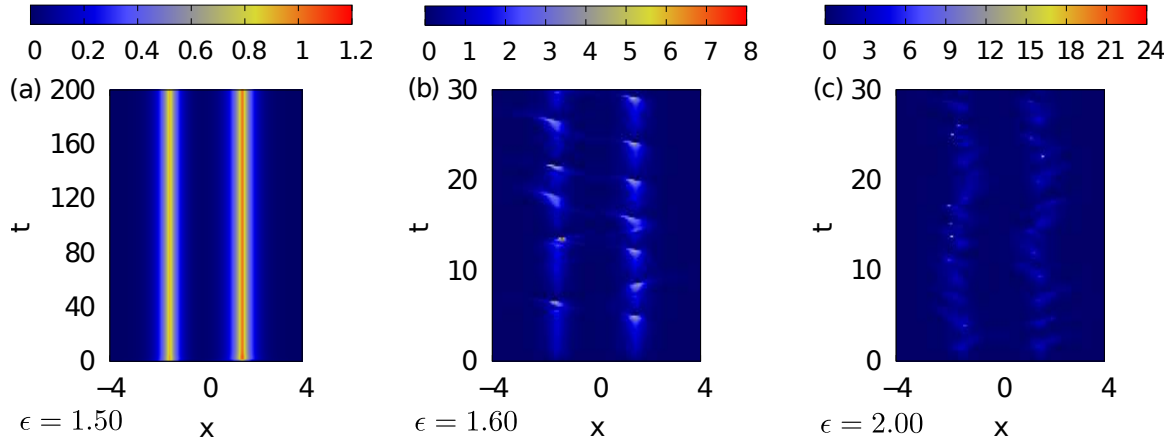


FIG. 23. (a) A stable bound state produced by the quintic LL equation (17) with the pump strength  $\epsilon = 1.50$ . (b,c) The increase of  $\epsilon$  to values 1.60 and 2.00 leads, severally, to the onset of moderate and strong instability of the bound state. Other parameters are  $\eta^4 = 1$ ,  $\alpha = 1$ ,  $\sigma = 1$ ,  $\chi = \pi/2$ , and  $l = 3$ .

$\pi$ , as well as in the absence of the loss term in the LL equation ( $\alpha = 0$ ). At  $0 < \chi < \pi$  and  $\alpha > 0$ , SB takes place in the linearized and nonlinear (self-focusing or defocusing) versions of the LL model alike, which is explained analytically. Families of stable symmetric and asymmetric bound states pinned to the double HS have been also found in the framework of the LL equation with the quintic self-focusing, in spite of the full instability of the TSs (Townes solitons) as solutions of the NLS equation with the same quintic nonlinearity.

As extension of the work, Ref. [31] suggests a challenging possibility to explore bound states, and the SB phenomenology in them, in terms of the two-dimensional LL equation with local pumps (in particular, vortical ones).

#### ACKNOWLEDGMENTS

W.B.C. acknowledges the financial support of the Brazilian agency CNPq (grant #306105/2022-5). This work was also performed as part of the Brazilian National Institute of Science and Technology (INCT) for Quantum Information (#465469/2014-0). The work of S.K. and B.A.M. is supported, in part, by the Israel Science Foundation through grant No. 1695/22.

- 
- [1] Y. S. Kivshar and G. Agrawal, *Optical Solitons: From Fibers to Photonic Crystals* (Elsevier Science, 2003).
  - [2] T. Dauxois and M. Peyrard, *Physics of Solitons* (Cambridge University Press, Cambridge, UK, 2006).
  - [3] N. N. Rosanov, *Spatial Hysteresis and Optical Patterns* (Springer: Berlin, 2002).
  - [4] M. F. S. Ferreira, *Dissipative Optical Solitons* (Springer Nature Switzerland AG, Cham, Switzerland, 2022).
  - [5] P. Grelu and N. Akhmediev, *Dissipative solitons for mode-locked lasers*, *Nature Phot.* **6**, 84-92 (2012).
  - [6] B. A. Malomed, *Multidimensional dissipative solitons and solitary vortices*, *Chaos Solitons Fract.* **163**, 112526 (2022).
  - [7] L. A. Lugiato and R. Lefever, *Spatial Dissipative Structures in Passive Optical Systems*, *Phys. Rev. Lett.* **58**, 2209 (1987).
  - [8] A. Coillet, I. Balakireva, R. Henriët, K. Saleh, L. Larger, J. M. Dudley, C. R. Menyuk, Y. K. Chembo, *Azimuthal Turing patterns, bright and dark cavity solitons in Kerr combs generated with whispering-gallery-mode resonators*, *IEEE Photon. J.* **5**, 6100409-6100409 (2013).
  - [9] M. Tlidi and K. Panajotov, *Two-dimensional dissipative rogue waves due to time-delayed feedback in cavity nonlinear optics*, *Chaos* **27**, 013119 (2017).
  - [10] K. Panajotov, M. G. Clerc, and M. Tlidi, *Spatiotemporal chaos and two-dimensional dissipative rogue waves in Lugiato-Lefever model*, *Eur. Phys. J. B* **71**, 176 (2017).
  - [11] M. Tlidi and M. Taki, *Rogue waves in nonlinear optics*, *Adv. Opt. Photon.* **14**, 87-147 (2022).
  - [12] Y. Sun, P. Parra-Rivas, F. Mangini, and S. Wabnitz, *Multidimensional localized states in externally driven Kerr cavities with a parabolic spatiotemporal potential: a dimensional connection*, *Chaos Solitons Fract.* **183**, 114870 (2024).
  - [13] G. J. de Valcárcel and K. Staliunas, *Phase-bistable Kerr cavity solitons and patterns*, *Phys. Rev. A* **87**, 043802 (2013).
  - [14] S. Coen, H. G. Randle, T. Sylvestre, and M. Erkintalo, *Modeling of octave-spanning Kerr frequency combs using a generalized mean-field Lugiato-Lefever model*, *Opt. Lett.* **38**, 37-39 (2013).

- [15] M. R. E. Lamont, Y. Okawachi, and A. L. Gaeta, [Route to stabilized ultrabroadband microresonator-based frequency combs](#), *Opt. Lett.* **38**, 3478-3481 (2013).
- [16] C. Godey, I. V. Balakireva, A. Coillet, and Y. K. Chembo, [Stability analysis of the spatiotemporal Lugiato-Lefever model for Kerr optical frequency combs in the anomalous and normal dispersion regimes](#), *Phys. Rev. A* **89**, 063814 (2014).
- [17] V. E. Lobanov, G. Lihachev, T. J. Kippenberg, and M. L. Gorodetsky, [Frequency combs and platicons in optical microresonators with normal GVD](#), *Opt. Exp.* **23**, 7713-7721 (2015).
- [18] M. Karpov, H. Guo, A. Kordts, V. Brasch, M. H. P. Pfeiffer, M. Zervas, M. Geiselmann, and T. J. Kippenberg, [Raman Self-Frequency Shift of Dissipative Kerr Solitons in an Optical Microresonator](#), *Phys. Rev. Lett.* **116**, 103902 (2016).
- [19] F. Copie, M. Conforti, A. Kudlinski, A. Mussot, and S. Trillo, [Competing Turing and Faraday Instabilities in longitudinally modulated passive resonators](#), *Phys. Rev. Lett.* **116**, 143901 (2016).
- [20] P. Parra-Rivas, D. Gomila, P. Colet, and L. Gelens, [Interaction of solitons and the formation of bound states in the generalized Lugiato-Lefever equation](#), *Eur. Phys. J. D* **71**, 198 (2017).
- [21] M. G. Clerc, M. A. Ferré, S. Coulibaly, R. G. Rojas, and M. Tlidi, [Chimera-like states in an array of coupled-waveguide resonators](#), *Opt. Lett.* **42**, 2906-2909 (2017).
- [22] B. Garbin, Y. Wang, S. G. Murdoch, G.-L. Oppo, S. Coen, and M. Erkintalo, [Experimental and numerical investigations of switching wave dynamics in a normally dispersive fibre ring resonator](#), *Eur. Phys. J. D* **71**, 240 (2017).
- [23] Q. Li, T. C. Briles, D. A. Westly, T. E. Drake, J. R. Stone, B. R. Ilic, S. A. Diddams, S. B. Papp, and K. Srinivasan, [Stably accessing octave-spanning microresonator frequency combs in the soliton regime](#), *Optica* **4**, 193-203 (2017).
- [24] Y. V. Kartashov, O. Alexander, and D. V. Skryabin, [Multistability and coexisting soliton combs in ring resonators: the Lugiato-Lefever approach](#), *Opt. Express* **25**, 11550-11555 (2017).
- [25] L. A. Lugiato, F. Prati, M. L. Gorodetsky, and T. J. Kippenberg, [From the Lugiato-Lefever equation to microresonator-based soliton Kerr frequency combs](#), *Phil. Trans. R. Soc. A* **376**, 20180113 (2018).
- [26] T. Daugey, C. Billet, J. Dudley, J.-M. Merolla, and Y. K. Chembo, [Kerr optical frequency comb generation using whispering-gallery-mode resonators in the pulsed-pump regime](#), *Phys. Rev. A* **103**, 023521 (2021).
- [27] X. Dong, C. Spiess, V. G. Bucklew, and W. H. Renninger, [Chirped-pulsed Kerr solitons in the Lugiato-Lefever equation with spectral filtering](#), *Phys. Rev. Research* **3**, 033252 (2021).
- [28] S.-W. Huang, J. Yang, S.-H. Yang, M. Yu, D.-L. Kwong, T. Zelevinsky, M. Jarrahi, and C. W. Wong, [Globally stable microresonator Turing pattern formation for coherent high-power THz radiation on-chip](#), *Phys. Rev. X* **7**, 041002 (2017).
- [29] W. B. Cardoso, L. Salasnich, and B. A. Malomed, [Localized solutions of Lugiato-Lefever equations with focused pump](#), *Sci. Rep.* **7**, 16876 (2017).
- [30] W. B. Cardoso, L. Salasnich, and B. A. Malomed, [Zero-dimensional limit of the two-dimensional Lugiato-Lefever equation](#), *Eur. Phys. J. D* **71**, 112 (2017).
- [31] S. Kumar, W. B. Cardoso, and B. A. Malomed, [Stable patterns in the Lugiato-Lefever equation with a confined vortex pump](#), *Symmetry* **16**, 470 (2024).
- [32] L. Bergé, [Wave collapse in physics: principles and applications to light and plasma waves](#), *Phys. Rep.* **303**, 259-370 (1998).
- [33] G. Fibich, [The Nonlinear Schrödinger Equation: Singular Solutions and Optical Collapse](#) (Springer, Heidelberg, 2015).
- [34] C.-K. Lam, B. A. Malomed, K. W. Chow, P. K. A. Wai, [Spatial solitons supported by localized gain in nonlinear optical waveguides](#), *Eur. Phys. J. Special Topics* **173**, 217 (2009).
- [35] C. H. Tsang, B. A. Malomed, C.-K. Lam, and K. W. Chow, [Solitons pinned to hot spots](#), *Eur. Phys. J. D* **59**, 81-89 (2010).
- [36] T. Mayteevarunyoo, B. A. Malomed, and G. Dong, [Spontaneous symmetry breaking in a nonlinear double-well structure](#), *Phys. Rev. A* **78**, 053601 (2008).
- [37] L. Khaykovich and B. A. Malomed, [Deviation from one dimensionality in stationary properties and collisional dynamics of matter-wave solitons](#), *Phys. Rev. A* **74**, 023607 (2006).
- [38] J. Yang, [Nonlinear waves in integrable and nonintegrable systems](#) (Society for Industrial and Applied Mathematics, Philadelphia, 2010).
- [39] G. Boudebs, S. Cherukulappurath, H. Leblond, J. Troles, F. Smektala, and F. Sanchez, [Experimental and theoretical study of higher-order nonlinearities in chalcogenide glasses](#), *Opt. Commun.* **219**, 427-433 (2003).
- [40] S. Konar, M. Mishra, and S. Jana, [Nonlinear evolution of cosh-Gaussian laser beams and generation of flat top spatial solitons in cubic quintic nonlinear media](#), *Phys. Lett. A* **362**, 505-510 (2007).
- [41] A. S. Reyna and C. B. de Araújo, [High-order optical nonlinearities in plasmonic nanocomposites – a review](#), *Ad. Opt. Phot.* **9**, 720-774 (2017).
- [42] A. S. Reyna and C. B. de Araújo, [Nonlinearity management of photonic composites and observation of spatial-modulation instability due to quintic nonlinearity](#), *Phys. Rev. A* **89**, 063803 (2014).
- [43] G. Kozyreff, [Localized Turing patterns in nonlinear optical cavities](#), *Physica D* **241**, 939-946 (2012).
- [44] G. R. Kol, [Controllable rogue waves in Lugiato-Lefever equation with higher-order nonlinearities and varying coefficients](#), *Opt. Quant. Elect.* **48**, 419 (2016).
- [45] F. Kh. Abdullaev and M. Salerno, [Gap-Townes solitons and localized excitations in low-dimensional Bose-Einstein condensates in optical lattices](#), *Phys. Rev. A* **72**, 033617 (2005).